

Construction of Highly Active and Selective Molecular Imprinting Catalyst for Hydrogenation

Dongcheng He, Teng Li, Xingchao Dai, Shujuan Liu, Xinjiang Cui,* and Feng Shi*



Cite This: *J. Am. Chem. Soc.* 2023, 145, 20813–20824



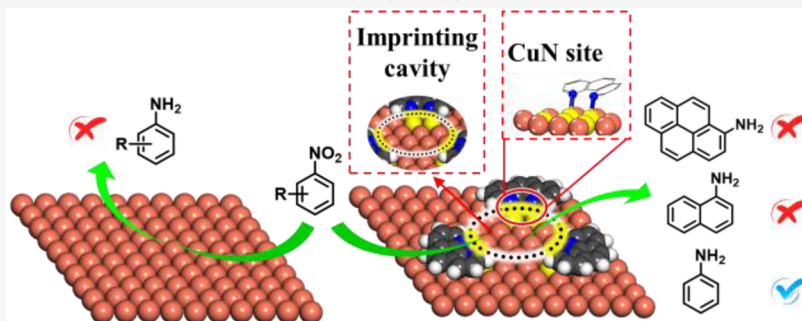
Read Online

ACCESS |

Metrics & More

Article Recommendations

Supporting Information



ABSTRACT: Surface molecular imprinting (MI) is one of the most efficient techniques to improve selectivity in a catalytic reaction. Heretofore, a prerequisite to fabricating selective catalysts by MI strategies is to sacrifice the number of surface-active sites, leading to a remarkable decrease of activity. Thus, it is highly desirable to design molecular imprinting catalysts (MICs) in which both the catalytic activity and selectivity are significantly enhanced. Herein, a series of MICs are prepared by sequentially adsorbing imprinting molecules (nitro compounds, N) and imprinting ligand (1,10-phenanthroline, L) over the copper surface of Cu/Al₂O₃. The resulting Cu/Al₂O₃-N-L MICs not only offer promoted catalytic selectivity but also enhance catalytic activity for nitro compounds hydrogenation by creating imprinting cavity derived from the presorption of N and forming new active Cu-N sites at the interface of the copper sites and L. Characterizations by means of various experimental investigations and DFT calculations disclose that the molecular imprinting effect (promoted activity and selectivity) originates from the formation of new active Cu-N sites and precise imprinting cavities, endowing promoted catalytic selectivity and activity on the hydrogenation of nitro compounds.

1. INTRODUCTION

High selectivity toward target products, achieved by promoting the favorable reaction pathways,¹ is one of the most important objectives in heterogeneous catalysis. Various strategies have been developed to improve catalytic selectivity. The concept of the shape selectivity where the precious access of reactants to uniform and regular pores and channels facilitates the formation of the desired products in maximum, has been widely studied using zeolite,^{2–5} metal–organic frameworks,⁶ and other materials.^{7,8} Enhancing the specific interaction between the active site and proceeding molecules is another approach to improve the selectivity which could be obtained by the fabrication of bimetallic,^{9,10} metal nanocatalysts,^{11–15} or modification of the metal support interaction.^{16–20} Control of selectivity could also be achieved by the design of the catalysts with specific individual active sites where the expected reaction pathway to the desired product would be ideally conducted, and protocols such as immobilizing homogeneous catalysts on solid surfaces,^{21–24} tailoring surface and interface structures of catalysts,^{25,26} and fabrication of single-site or single-atom heterogeneous catalysts^{27–30} have been emerged for this purpose.

Recently, molecular imprinting strategies have been received increasing attention for chemo/biosensing,^{31,32} biological binding assays,^{33,34} and particularly in catalysis,³⁵ by the rational manufacture of materials with predictable structure, specific imprinting sites, and universal utilization.^{32,36,37} In catalysis, the control of reaction selectivity could be achieved by the fabrication of catalysts with specific imprinting site/cavity that benefits the reactant adsorption and desired product desorption.

Tremendous efforts have been made to accomplish enhanced catalytic selectivity by molecular imprinting (MI), and several strategies have been developed to synthesize MICs on metal supported heterogeneous catalysts. For example, the MICs were fabricated by covering undesired active sites with toxic molecules or metal oxides shell and forming imprinting

Received: May 3, 2023

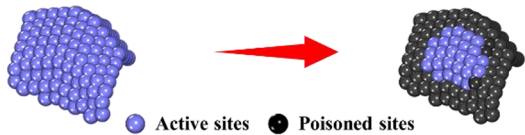
Published: September 18, 2023



cavity to adsorb the reactant, endowing promoted catalytic selectivity of the heterogeneous catalysts (Figure 1a). A

High selectivity with low activity realized by poisoning the active sites

a: poisoning active sites



High selectivity with activity achieved by creating imprinting cavity and new active sites

b: this work

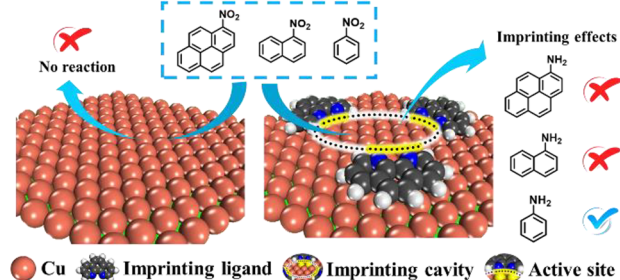


Figure 1. Comparison of traditional MI strategies with ours in this work. Improved catalytic selectivity by traditional MI strategies of (a) covering part of the active sites with toxic molecules or metal oxides. Enhanced catalytic activity and selectivity by our protocol of (b) imprinting molecules (nitro compounds) and the imprinting ligand (1,10-phenanthroline) triggered MICs.

sequential adsorption strategy has been reported where the metal surface is selectively absorbed by an aromatic imprinting molecule and subsequently poisoned by dimethylaminopropylamine, resulting in an imprinting cavity for effective hydrogenation of aromatics.³⁸ Similarly, MICs with special imprinting cavity could also be obtained by similar sequential methods by replacing the organic adsorbent with metal oxides.³⁹

However, the MICs in Figure 1a can easily deactivate the catalyst if the poisoning process for the imprinting molecule or metal oxide shell growth is not well controlled. More seriously, a prerequisite to fabricating the imprinting site/cavity by these MI strategies *vide supra* is to sacrifice the number of surface-active sites, thereby resulting in the loss of activity. Thus, it is highly desirable to design MICs which both the catalytic activity and selectivity are enhanced.

The key step to design the catalyst with promoted activity and selectivity over the metal surface by MI strategies is to fabricate the imprinting cavity and simultaneously generate a new highly active site by coordinating with imprinting ligands. By binding with surface metal sites of nanoparticles, *N*-heterocyclic carbenes (NHCs) not only stabilized the metal sites but also generated new active species.^{40,41} For example, Glorius and co-workers exhibited an activating effect of NHCs on surfaces of heterogeneous catalysts, achieving promoted catalytic performance on coupling reactions, hydrogenation, and others.⁴² Clearly, the model imprinting ligand should have optimal coordination rather than an irreversible poisoning strong interaction with surface metal, producing new active sites for the adsorption and activation of reactant molecules. For this case, the *N*-containing ligands are considered as preferable candidates because their coordination with metal centers is not as strong as that by iodine and sulfur imprinting

molecules.⁴⁰ Meanwhile, it is ideal to use the reactant molecules directly as the imprinting molecule to fabricate the exclusive imprinting cavity, preventing the adsorption of undesirable substrate with even a tiny structure difference.

Inspired by the discussions *vide supra*, we demonstrated a strategy to fabricate Cu-MICs that simultaneously enhance both catalytic activity and selectivity significantly for nitro compounds hydrogenation. The Cu-MICs were synthesized by a sequential adsorption of imprinting molecules (nitro compounds, N₁) and imprinting ligand (1,10-phenanthroline, L₁) over the surface of Cu nanoparticles (Figure 1b). The resulting MICs displayed exclusively molecular imprinting effects (promoted activity and selectivity) toward the hydrogenation of imprinting nitro compound molecules but quite low activity for other substrates with even subtle structure difference. The superior molecular imprinting effect of the resulting MICs was ascribed to the formation of new active Cu-N sites and precise imprinting cavities. Our work provided a new strategy to synthesize MICs with the architectures of both new active sites and precise imprinting cavities, resulting in promoted catalytic activity and selectivity.

2. EXPERIMENTAL SECTION

2.1. Synthesis of MICs over Cu/Al₂O₃ (Cu/Al₂O₃-N-L). The synthesis of the MICs followed the schematic in Figure 2a, and the nitrobenzene (N₁) and prepared Cu/Al₂O₃ were separately placed in two porcelain boats located at upstream and downstream directions in a tube furnace at 150 °C for 2 h under flowing 10% H₂/Ar gas. The resulting Cu/Al₂O₃-N₁ modified by adsorbing nitro compounds further adsorbed the 1,10-phenanthroline (L₁) using the similar methodology at 130 °C for 2 h to yield the MIC named as Cu/Al₂O₃-N₁-L₁ downstream, where N₁ and L₁ are denoted as the imprinting nitro compounds and imprinting ligands, respectively. Similarly, the MICs of Cu/Al₂O₃-N₂-L₁ (N₂: 1-nitronaphthalene) and Cu/Al₂O₃-N₃-L₁ (N₃: 1-nitropyrene) with 1,10-phenanthroline were prepared.

2.2. Physical Characterizations. To shed light on the origin of the above successes, various characterizations were conducted to study the structures of all MICs samples, such as inductively coupled plasma atomic emission spectroscopy (ICP-AES), N₂ adsorption-desorption analysis, X-ray powder diffraction (XRD), X-ray photoelectron spectroscopy (XPS), transmission electron microscopy (TEM), IR-diffuse reflectance spectrum (IR), UV-Raman spectrum (UV-Raman), thermogravimetric analysis (TGA), element analyses (EA), auger electron spectroscopy (AES), X-ray absorption fine structure (XAFS), H₂-TPR, N₂O pulse adsorption, and DFT calculations. For details about the characterization instruments and parameters are in support information.

2.3. Computational Method and Details. All calculations were preceded on the basis of a periodic slab model by using the density functional theory method implemented in the Vienna Ab initio Simulation Package (VASP). The projected augmented wave method (PAW) was used to describe the interaction of the electron and ion. The electron exchange and correlation energies were calculated within the generalized gradient approximation method (GGA) by using the Perdew–Burke–Ernzerhof (PBE) functional. The value of the cutoff energy for plane wave basis was set up to 500 eV.

To make sure that the energy difference is less than 10⁻⁴ eV and that the force per atom is less than 0.03 eV/Å, second-order Methfessel–Paxton electron smearing (0.2 eV) was used. Dispersion correction was considered by using DFT-D3 method with Becke-Jonson damping. The vacuum layer between the periodically repeated slabs was set as 18 Å. Gamma point was set for sampling at Brillouin zone.

The adsorption energy (E_{ads}) of adsorbate (X) is obtained from the equation $E_{\text{ads}} = E_{X/\text{slab}} - E_{\text{slab}} - E_X$, where $E_{X/\text{slab}}$ is the total energy of the slab with adsorbate on it (after adsorption), E_{slab} is the total energy of the clean adsorbent slab and E_X is the total energy of the

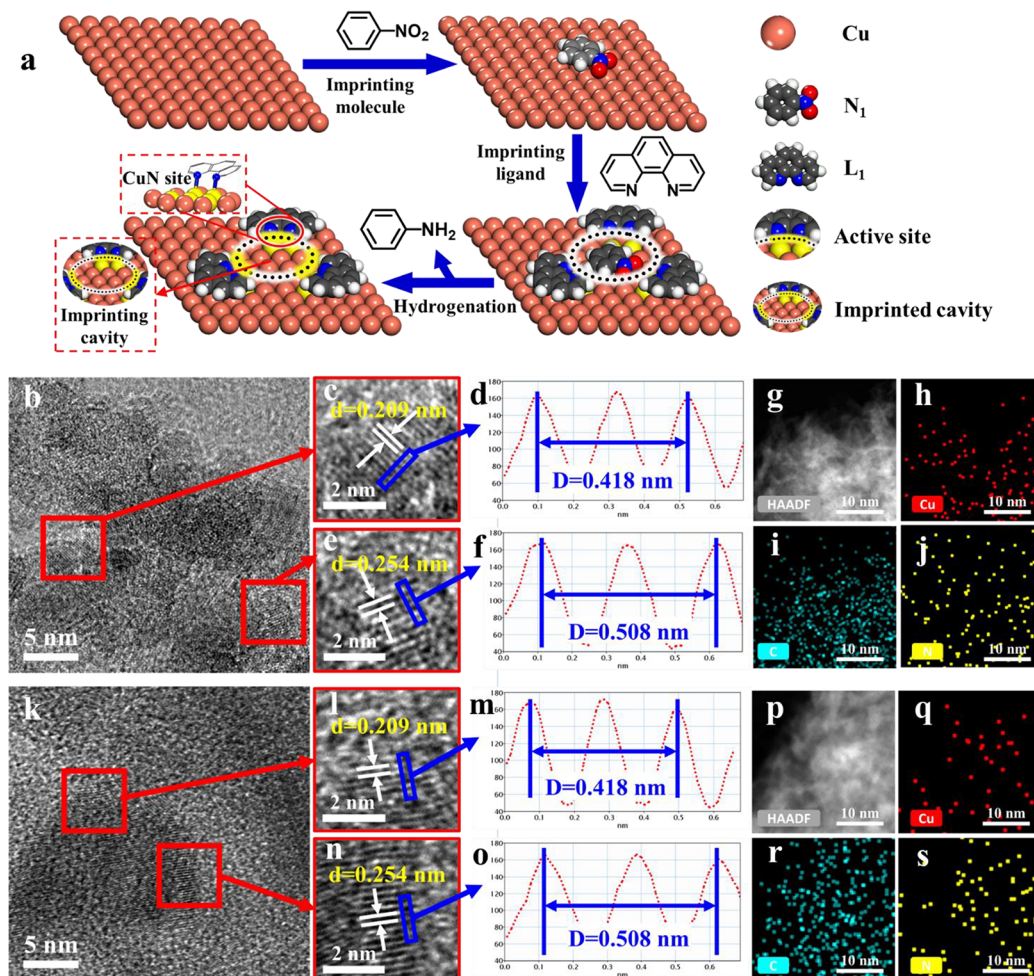


Figure 2. Diagram of preparation for $\text{Cu}/\text{Al}_2\text{O}_3\text{-N}_1\text{-L}_1$ and the TEM results for $\text{Cu}/\text{Al}_2\text{O}_3\text{-N}_1\text{-L}_1$ and $\text{Cu}/\text{Al}_2\text{O}_3\text{-N}_1\text{-L}_1$ used. (a) Schematic diagram of MICs preparation. (b) HR-TEM images, (c) and (e) Magnified pictures of red region from (b). (d) and (f) lattice distances of the blue region from (c) and (e). (g–j) elemental EDXS mapping of $\text{Cu}/\text{Al}_2\text{O}_3\text{-N}_1\text{-L}_1$. (k) HR-TEM images, (l) and (n) magnified pictures of red region from (k). (m) and (o) Lattice distance of blue region from (l) and (n). (p–s) Elemental EDXS mapping of $\text{Cu}/\text{Al}_2\text{O}_3\text{-N}_1\text{-L}_1$ -used.

free adsorbate (X) in gas phase; therefore, the more negative the E_{ads} , the higher (or stronger) the interactions between the adsorbates and surface. For reactions, the climbing-image nudged elastic band (CINEB) method was adopted to search the transition states (TS) of hydrogen dissociation, and the vibrational frequency analysis was also processed to verify the authentic transition state with only one imaginary frequency. The reaction barrier (E_a) is defined as $E_a = E_{\text{TS}} - E_{\text{IS}}$, and the reaction energy (E_r) is defined as $E_r = E_{\text{FS}} - E_{\text{IS}}$, where E_{IS} , E_{FS} , and E_{TS} are the total energies of the initial, final, and transition states, respectively.

The model with the (6×9) supercell was built to simulate the adsorption of related molecules separately. The (9×9) supercell was adopted to study the molecular imprint effect induced by nitronaphthalene, and the (12×12) supercell was adopted to study the molecular imprint effect caused by 1-nitropyrene, similarly.

2.4. Catalytic Performance Test. A mixture of nitrobenzene (1 mmol) and 80 mg of catalyst was added to a glass tube which was placed in a 100 mL autoclave, and then the autoclave was sealed and exchanged with H_2 three times and reacted at 120°C under 1.5 MPa H_2 for 12 h using $\text{Cu}/\text{Al}_2\text{O}_3\text{-N}_1\text{-L}_1$ as the catalyst. After the reaction, the autoclave was cooled to room temperature and the pressure was carefully released. Subsequently, the reaction mixture was diluted by 5 mL of toluene with 40 mg of biphenyl as internal standard for quantitative analysis by GC-FID (Agilent 7890B-5977A). Finally, the catalyst was separated from the reaction mixtures by centrifuging and washed with methylbenzene for three times. Other reactions and control experiments were tested in the same way.

2.5. Procedure for Recycling Test. The used catalyst was separated from the reaction mixtures by simple centrifugation and washed three times using methylbenzene. After being dried under vacuum at 80°C , it was recovered and directly recharged into the autoclave for the next run.

3. RESULTS AND DISCUSSION

3.1. Optimization of MICs. Series of Cu-MICs were synthesized using different imprinting molecules and imprinting ligands, as shown in Table 1. All the catalytic performance of the prepared Cu-MICs were tested for the molecular imprinting effects on the hydrogenation of nitro compounds in toluene. Clearly, bare $\text{Cu}/\text{Al}_2\text{O}_3$ without any modification displayed no activity on the hydrogenation of N_1 to N_3 (Table 1, entry 1). After using N_1 as imprinting molecule, the resulting catalysts were still not active (Table 1, entry 2), while the $\text{Cu}/\text{Al}_2\text{O}_3\text{-L}_1$ catalyst offered moderate yields of amines. However, no molecule imprinting effect was observed for N_1 to N_3 (Table 1, entry 3). Although this result indicated the formation of new active sites over the Cu surface formed in the presence of imprinting ligands, the disordered adsorption of L_1 failed to fabricate the imprinting cavity, leading the poor selectivity toward the hydrogenation of N_1 to N_3 . Surprisingly, the $\text{Cu}/\text{Al}_2\text{O}_3\text{-N}_1\text{-L}_1$ catalyst exhibited significant improvement on the

Table 1. Series of MICs Used for Various Nitro Compounds

RNO ₂	+ H ₂	Catalysts	120 °C, 12 h	RNH ₂
Imprinting molecules:				
N ₁ Nitrobenzene	N ₂ 1-Nitronaphthalene	N ₃ 1-Nitropyrene		
Imprinting ligands:				
L ₁ 1,10-Phenanthroline	L ₂ 1,7-Phenanthroline	L ₃ 4,7-Phenanthroline	L ₄ 2,2'-Bipyridine	L ₅ Pyridine
Entry		Yields of different nitro-compounds to amines ^a		
Catalysts				
1	Cu/Al ₂ O ₃	0	0	0
2	Cu/Al ₂ O ₃ -N ₁	0	0	0
3	Cu/Al ₂ O ₃ -L ₁	84	51	63
4	Cu/Al ₂ O ₃ -N ₁ -L ₁	93	0	0
5	Cu/Al ₂ O ₃ -N ₂ -L ₁	5	93	0
6	Cu/Al ₂ O ₃ -N ₃ -L ₁	0	0	99
7	Cu/Al ₂ O ₃ -N ₁ -L ₂	0	0	0
8	Cu/Al ₂ O ₃ -N ₁ -L ₃	0	0	0
9	Cu/Al ₂ O ₃ -N ₁ -L ₄	0	0	0
10	Cu/Al ₂ O ₃ -N ₁ -L ₅	0	0	0
11	Fe/Al ₂ O ₃ -N ₁ -L ₁	0	0	0
12	Co/Al ₂ O ₃ -N ₁ -L ₁	0	0	0
13	Ni/Al ₂ O ₃ -N ₁ -L ₁	0	0	0

^aAll yields of nitro compounds to anilines were determined by calibrated GC-FID using diphenyl as standard. Reaction condition: nitro compound (1 mmol), catalyst (80 mg, 4.2 wt % Cu), toluene (4 mL), 1.5 MPa H₂, 120 °C, 12 h.

catalytic activity with 93% yield (Table 1, entry 4). More importantly, no hydrogenations of N₂ and N₃ were observed by Cu/Al₂O₃-N₁-L₁, indicating an expected molecular imprinting effect for the selective hydrogenations of various nitro compounds by the subsequent adsorption of N₁ and L₁. This phenomenon was further verified by using N₂ and N₃ as imprinting molecules where the resulting Cu/Al₂O₃-N₂-L₁ and Cu/Al₂O₃-N₃-L₁ can only hydrogenated the N₂ and N₃, respectively rather than other substrates (Table 1, entries 5 and 6). These results strongly confirmed the fabrication of an imprinting cavity on the surface of Cu nanoparticles where the adsorption and activation of substrates with mismatched size and shape were efficiently blocked by the imprinting cavity. New active sites were created in the presence for L₁, endowing them highly improved catalytic activity.

Note that the Cu/Al₂O₃-N₁-L₁ displayed outperformed reactivity compared with other similar imprinting ligand such as 1,7-phenanthroline (L₂) and 4,7-phenanthroline (L₃) on the hydrogenation of nitrobenzene under the identical conditions (Table 1, entries 7 and 8). Therefore, even subtle structural

changes in L led to tremendous loss of activity and selectivity. As expected, the MICs synthesized using more different imprinting ligand such as pyridine (L₄) and 2,2'-bipyridine (L₅) exhibited no activity toward the hydrogenation of N₁ (Table 1, entries 9 and 10). Moreover, similar catalysts with different metals, such as Fe/Al₂O₃-N₁-L₁, Co/Al₂O₃-N₁-L₁, and Ni/Al₂O₃-N₁-L₁, were obtained by the same preparation method but showed no activity for the hydrogenation of N₁ (Table 1, entries 11–13). The effect of adsorption temperature over N₁ and L₁ for the catalytic performance was studied as in Table S4. After careful investigation, the optimal adsorption temperatures for N₁ and L₁ were 150 and 130 °C respectively.

3.2. Characterization of Catalysts. According to the above experimental analysis, an outstanding imprinting effect with enhanced catalytic activity and selectivity on nitrobenzene hydrogenation was successfully achieved. To shed light on the origin of the above successes, various characterizations were conducted to study the structures of all MICs samples. High-resolution transmission electron microscopy (HR-TEM) images of bare Cu/Al₂O₃ showed the presence of metallic Cu nanoparticles with a characteristic spacing of 0.207 nm for Cu(111) (Figure S1). After adsorption of the imprinting molecule (N₁) and imprinting ligand (L₁), the lattice fringe for Cu(111) in Cu/Al₂O₃-N₁-L₁ was slightly increased to 0.209 nm (Figure 2b–d), indicating the interaction between the Cu sites with N₁ or L₁ and electron transfer from Cu to L₁. Meanwhile, the EDS mapping images revealed the presence of Cu nanoparticles and the dispersion of C and N on the surface of the catalyst, confirming the adsorption of imprinting molecule and imprinting ligand (Figure 2g–j). As shown in Figure 2k–m, the TEM images of used Cu/Al₂O₃-N₁-L₁ displayed that the lattice fringe of Cu(111) was 0.209 nm which was identical with Cu/Al₂O₃-N₁-L₁, indicating the stable nature of the catalysts during the reaction.

Considering the existence of L₁ after hydrogenation reaction confirmed by the IR and UV-Raman analysis (Figures 3b and S3b), we strongly believed the expansion of the lattice fringe of Cu(111) was caused by the interaction of Cu sites with L₁ rather than N₁. Interestingly, a characteristic spacing of 0.254 nm was observed for Cu/Al₂O₃-N₁-L₁ and Cu/Al₂O₃-N₁-L₁-used, which can be attributed to Cu-N sites (Figures 2e,f and 2n,o).

Using other nitro compounds as imprinting molecule, such as 1-nitronaphthalene (N₂) and 1-nitropyrene (N₃), the resulting Cu/Al₂O₃-N₂-L₁ and Cu/Al₂O₃-N₃-L₁ MICs also exhibited the lattice fringe for Cu-N sites, indicating the generality of this strategy to synthesis of MICs using different imprinting molecules (Figure S2).

Thermogravimetric analysis (TGA) was conducted to clarify the successful adsorption of N₁ and L₁. Figure 3a shows that the weight loss for Cu/Al₂O₃-N₁, Cu/Al₂O₃-L₁, and Cu/Al₂O₃-N₁-L₁ were 4.4%, 12.5%, and 10.0% respectively. It is worth noting that the mass loss of Cu/Al₂O₃-L₁ was higher than that of Cu/Al₂O₃-N₁-L₁, suggesting the preadsorption of nitrobenzene inhibited the adsorption capacity of L₁. Although more L₁ were existed on the surface of Cu/Al₂O₃-L₁, no molecular imprinting effects was tested due to the disordered adsorption of L₁, confirming the high importance of imprinting molecule N₁ on the formation of the imprinting cavity. In addition, the surface areas for Cu/Al₂O₃-N₁, Cu/Al₂O₃-L₁ and Cu/Al₂O₃-N₁-L₁ decreased compared with bare Cu/Al₂O₃, confirming the absorption of N₁ and L₁ (Table S5 and Figure S5). As shown in Table S6, a 16% yield was achieved without

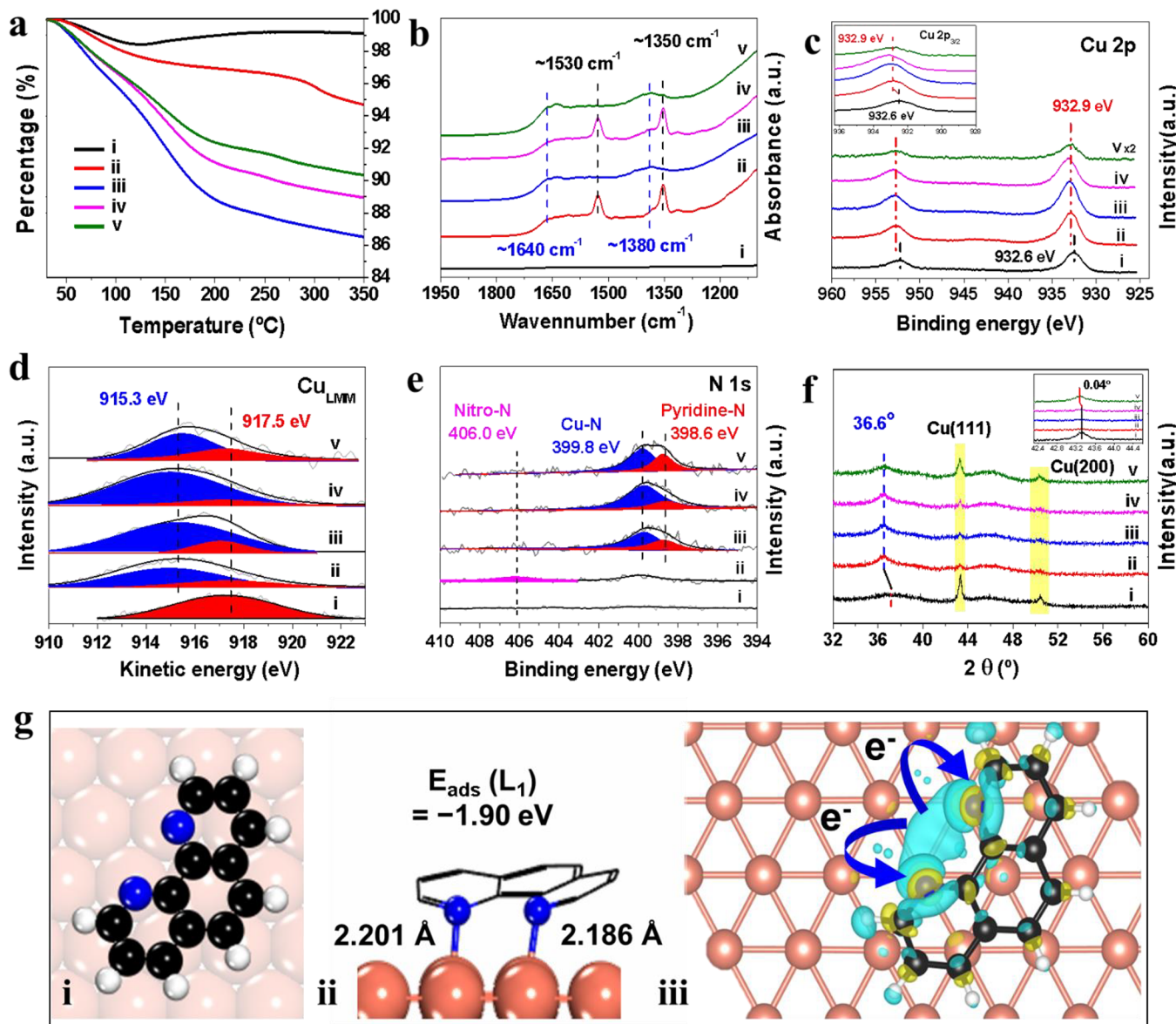


Figure 3. Characterizations of MICs samples and compared catalysts. (a) TGA analysis of catalysts of i–v. (b) IR-diffuse reflectance spectrum of catalysts treatment process. (c) XPS of Cu 2p of Cu/Al₂O₃ and MICs catalysts. (d) AES of Cu_{LMM} of Cu/Al₂O₃ and MICs catalysts, (e) XPS of N 1s of MICs, (f) XRD patterns of Cu/Al₂O₃ and treated catalysts (i, Cu/Al₂O₃, ii, Cu/Al₂O₃-N₁, iii, Cu/Al₂O₃-L₁, iv, Cu/Al₂O₃-N₁-L₁, v, Cu/Al₂O₃-N₁-L₁-used). (g) Models of L1 adsorption on Cu(111) and electron density difference (H in white, C in black, N in blue, and Cu in orange).

any solvents. Thus, the influence of solvent on reaction was investigated in hydrogenation and highest yield was obtained in the presence of toluene. Moreover, the concentration of nitrobenzene was studied and highest yield was achieved using 4 mL of toluene. **Figure 3**

The molecule imprinting process was further monitored by IR-diffuse reflectance spectrum analysis, as shown in **Figure 3b**. Compared with bare Cu/Al₂O₃ catalyst (**Figure 3b**, curve (i)), two new noticeable adsorption peaks at 1,530 and 1,350 cm⁻¹ which was attributed to the N=O stretching and antistretching vibrations of nitro group, appeared after only adsorbing N₁ on Cu/Al₂O₃ (**Figure 3b**, curve (ii)). In addition, an adsorption peaks at 1,380 cm⁻¹ which assigned to the breathing vibrations of C=N of the L₁ was observed for Cu/Al₂O₃-L₁ (**Figure 3b**, curve (iii)). Subsequently, the Cu/Al₂O₃-N₁-L₁ catalyst after adsorbing both N₁ and L₁ were tested where all of the above-mentioned characteristic peaks

for N₁ and L₁ were detected (**Figure 3b**, curve (iv)), indicating the successful construction of the Cu/Al₂O₃-N₁-L₁ catalyst. Notably, when Cu/Al₂O₃-N₁-L₁ catalyst was used for N₁ hydrogenation in the presence of hydrogen at 120 °C, the intensity of the peak at 1,530 and 1,350 cm⁻¹ decreased substantially whereas the peaks at 1,640 and 1,380 cm⁻¹ were unaffected (**Figure 3b**, curve (v)). These results indicated that adsorbed N₁ as a template molecule temporarily existed on the surface of the catalyst and easily converted and released from the surface of Cu/Al₂O₃-N₁-L₁, whereas L₁ was still stable on the surface during the reaction. This was further confirmed by UV-Raman spectroscopy, where almost the same peaks were obtained for Cu/Al₂O₃-L₁ and recycled Cu/Al₂O₃-N₁-L₁ (**Figure S3b**). Similar phenomenon was obtained for Cu/Al₂O₃-N₂-L₁ and Cu/Al₂O₃-N₃-L₁ (**Figure S3c,d**). These results indicated that the interaction occurred at Cu/L₁ rather than Cu/N₁. Due to the easy interaction between surface Cu

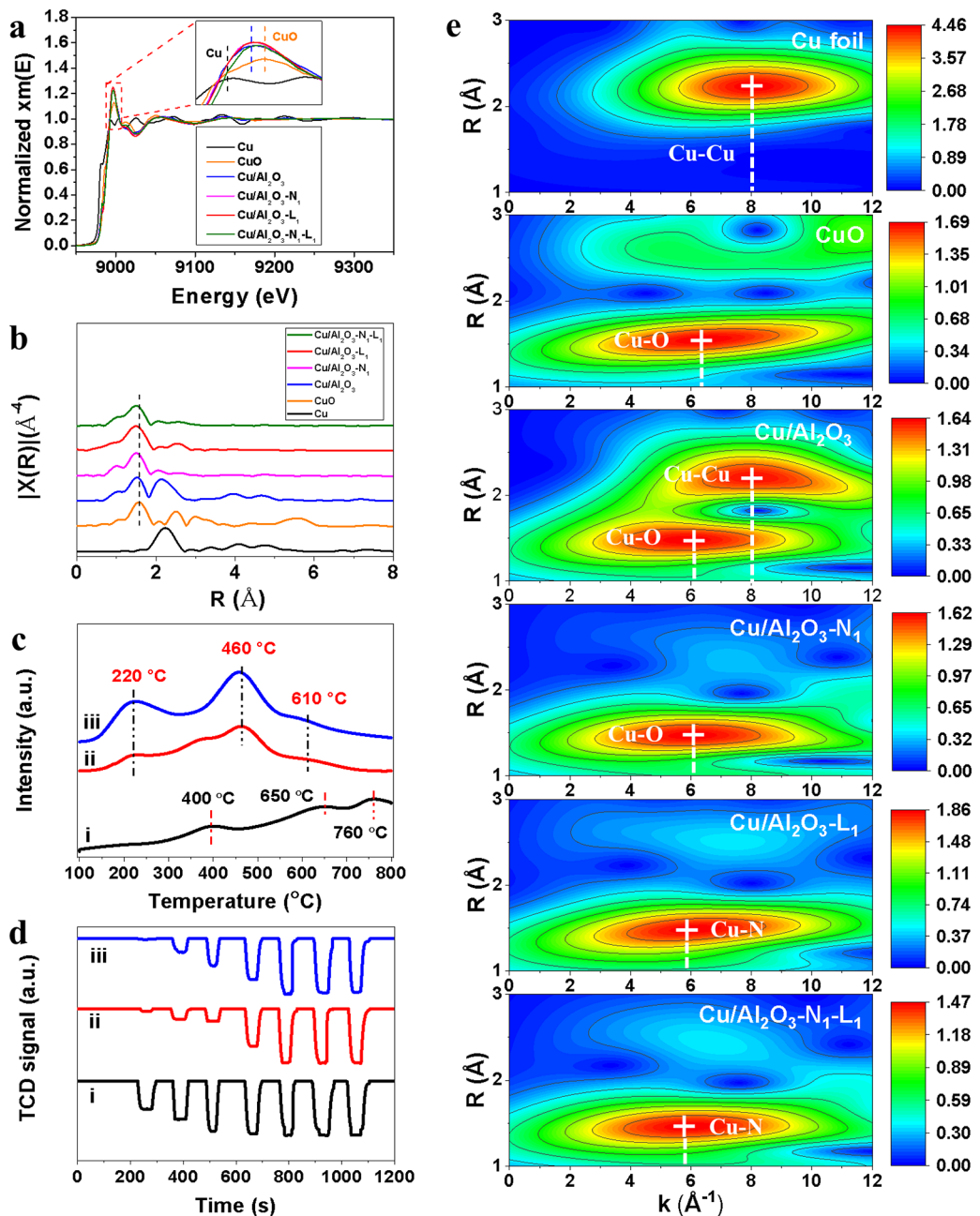


Figure 4. Characterizations of catalysts: (a) XANES spectra of catalysts, (b) Fourier transform at the Cu K-edge of catalysts. (c) $\text{H}_2\text{-TPR}$, (d) N_2O pulse (i, $\text{Cu}/\text{Al}_2\text{O}_3$; ii, $\text{Cu}/\text{Al}_2\text{O}_3\text{-N}_1\text{-L}_1$; iii, $\text{Cu}/\text{Al}_2\text{O}_3\text{-N}_1\text{-L}_1$ -used). (e) Wavelet transforms.

sites with N species of L_1 ,^{43,44} thereby we believed that new active Cu-N sites for the nitro compounds hydrogenation were created by the MI strategy, promoting the catalytic activity on nitro compound hydrogenation. Meanwhile, the easy desorption of the amine products recovered the imprinting cavity for the adsorption and hydrogenation of another molecular. The changes in chemical states and surface compositions of MICs were studied by X-ray photoelectron spectroscopy (XPS). The C 1s of all MICs showed an obvious characteristic peak of carbon at 284.7 eV, while a N 1s signal peak at 399.4 eV was simultaneously observed, indicating the successful adsorption of nitro compounds or/and 1,10-phenanthroline (Figure S6a,b). The binding energies (BEs) of Cu 2p for $\text{Cu}/\text{Al}_2\text{O}_3\text{-N}_1$, $\text{Cu}/\text{Al}_2\text{O}_3\text{-L}_1$, and $\text{Cu}/\text{Al}_2\text{O}_3\text{-N}_1\text{-L}_1$ were located at 932.9 eV and shift higher values of 0.3 eV compared with that in bare

$\text{Cu}/\text{Al}_2\text{O}_3$ (Figure 3c), suggesting the interaction of Cu with L_1 and the electronic transfer from Cu to L_1 . Similar results were obtained for $\text{Cu}/\text{Al}_2\text{O}_3\text{-N}_2\text{-L}_1$ and $\text{Cu}/\text{Al}_2\text{O}_3\text{-N}_3\text{-L}_1$ (Figure S6c,d). The auger electron spectroscopy (AES) further confirmed the electron modification from Cu to L_1 (Figure 3d). Obviously, the kinetic energy of Cu_{LMM} peak around 917.5 eV was attributed to Cu^0 for $\text{Cu}/\text{Al}_2\text{O}_3$ (Figure 3d, curve (i)), while the peak around 915.3 eV was ascribed to positively charged Cu species ($\text{Cu}^{\delta+}$) for $\text{Cu}/\text{Al}_2\text{O}_3\text{-N}_1$, $\text{Cu}/\text{Al}_2\text{O}_3\text{-L}_1$, and $\text{Cu}/\text{Al}_2\text{O}_3\text{-N}_1\text{-L}_1$ (Figure 3d, curves ii–iv),^{45,46} indicating the surface electron transfer from Cu to N species of L_1 . Besides, AES of $\text{Cu}/\text{Al}_2\text{O}_3\text{-N}_2\text{-L}_1$ and $\text{Cu}/\text{Al}_2\text{O}_3\text{-N}_3\text{-L}_1$ also obtained similar results (Figure S6e,f) where the kinetic energy shift after adsorbing L_1 verified the electrons export from Cu species due to the coordination of Cu sites with N species. The

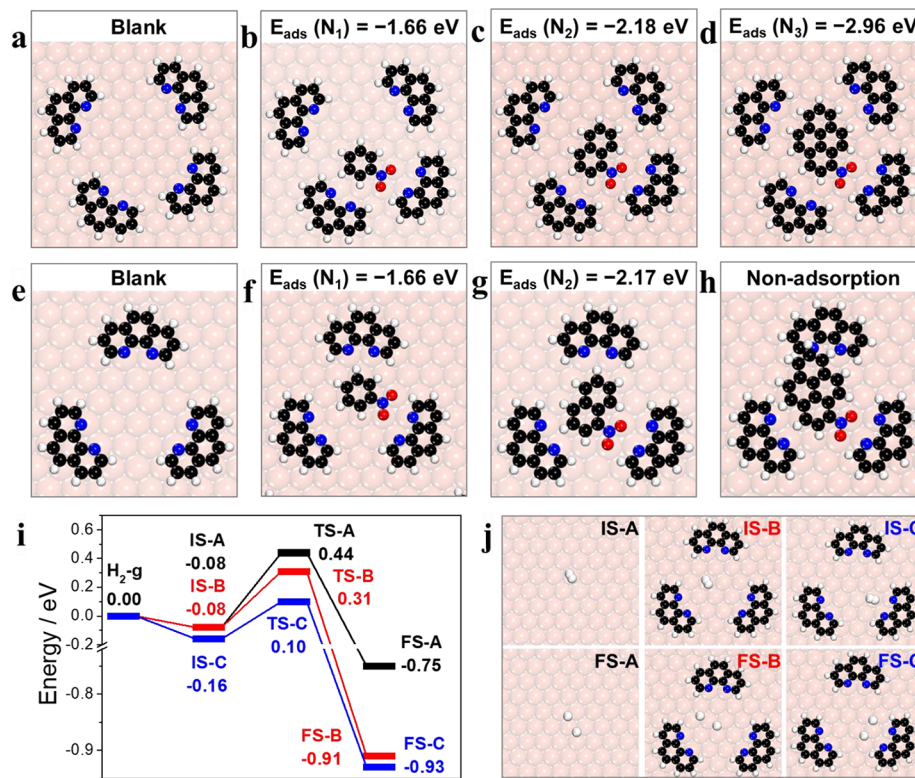


Figure 5. The adsorption energy (E_{ads}) of N on imprinting cavity model and the adsorption energy of H₂ on different positions: (a) blank, (b) N₁, (c) N₂, and (d) N₃ on Cu/Al₂O₃-N₃-L₁ catalyst. (e) Blank, (f) N₁, (g) N₂, (h) N₃ on Cu/Al₂O₃-N₂-L₁ catalyst. (i) Energy profiles of H₂ activation on the imprinting cavity of the Cu/Al₂O₃-N₁-L₁ catalyst: black, H₂ on bare Cu(111) (IS-A); orange, H₂ on the imprinting cavity far from L₁ (IS-B); blue, H₂ on the imprinting cavity closed to L₁ (IS-C). (j) Diagram of H₂ on pure Cu(111) and imprinting cavity (H in white, C in black, O in red, N in blue, and Cu in orange).

high-resolution XPS spectrum of N 1s for Cu/Al₂O₃-L₁ and Cu/Al₂O₃-N₁-L₁ can be deconvoluted into 398.6 and 399.8 eV, which were consistent with pyridinic N from L₁ and Cu-N, respectively (Figure 3e).^{43,47} The appearance of the Cu-N characteristic peak indicated the coordination of Cu sites with N species. In addition, XPS spectrum of N 1s displayed no obvious change for the used Cu/Al₂O₃-N₁-L₁, suggesting the stable nature of the Cu-N sites during the hydrogenation.

Thereafter, the bare Cu/Al₂O₃ catalyst and all MICs samples were characterized by X-ray powder diffraction measurement (XRD). As shown in Figure 3f, two peaks appearing at 43.3° and 50.4° for fresh Cu/Al₂O₃ respectively corresponded to (111) and (200) of Cu (PDF no. 99-0034). Note that these two peaks were remarkably weakened because both N₁ and L₁ were covered on the surface of copper during the preparation of fresh Cu/Al₂O₃-N₁-L₁ (Figure 3f, curves (ii–iv)). However, after the hydrogenation, N₁ was transformed into aniline and desorbed from copper, leading the exposure of the surface copper and the increase of Cu(111) diffraction peaks for Cu/Al₂O₃-N₁-L₁-used (Figure 3f, curve (v)). Interestingly, the peaks of Cu(111) and Cu(200) peak at 43.3° and 50.4° were reappeared for the used Cu/Al₂O₃-N₁-L₁ catalyst, but the peak of Cu(111) had slightly left-shifted compared with the Cu/Al₂O₃ (Figure 3f), ascribing to the recovery of the imprinting cavities. Because the removal of N₁ and existence of L₁ after hydrogenation had been confirmed by IR-DRS and TGA vide supra, we assumed that the expansion of lattice spacing of Cu(111) was ascribed to the interaction of surface Cu sites with L₁. Notably, a new peak at 36.6° which was assigned to Cu-N sites (PDF no. 21-0281) was observed for Cu/Al₂O₃-

L₁, Cu/Al₂O₃-N₁-L₁, and Cu/Al₂O₃-N₁-L₁-used, further confirming the presence of interaction between the Cu and N species of L₁ and indicating the stability of Cu-N sites during the reaction.

DFT calculation disclosed the formation of a new bond of Cu-N between surface Cu and N species of L₁ based on the models of L₁ on Cu(111). As shown in Figure 3g, electron density difference analysis showed that the Cu species presented a state of electron depletion (cyan contours) and the N atomic from L₁ displayed electron accumulation (yellow contours), proving the electron transfer from Cu to L₁.

XAFS measurements were performed to analyze the coordination environment of Cu at the atomic level. Figure 4a showed the Cu K-edge X-ray absorption near-edge structure (XANES) spectra of Cu/Al₂O₃-N₁-L₁ as well as references including Cu foil and CuO. The absorption edge of Cu/Al₂O₃-N₁-L₁ was between Cu and CuO, indicating that Cu atoms were positively charged, consistent with the results of AES in Figure 3d. Furthermore, Fourier transform (FT) k^3 -weighted extended XAFS (EXAFS) fittings were carried out to obtain the structural parameters and extract the quantitative chemical configuration of Cu atoms in Cu/Al₂O₃-N₁-L₁. EXAFS spectrum of Cu/Al₂O₃-N₁-L₁ showed the Cu-N peak at 1.5 Å (Figure 4b). The coordination number of Cu-N in Cu/Al₂O₃-N₁-L₁ was ~3 (Table S7). The EXAFS spectra for Cu/Al₂O₃-N₂-L₁ and Cu/Al₂O₃-N₃-L₁ also obtained similar information to support the above results (Figure S8). Wavelet transform (WT) was used to analyze Cu K-edge EXAFS oscillations, as shown in Figure 4e. The WT maximums at 5.9 Å⁻¹ for Cu/Al₂O₃-L₁ and Cu/Al₂O₃-N₁-L₁ were assigned to

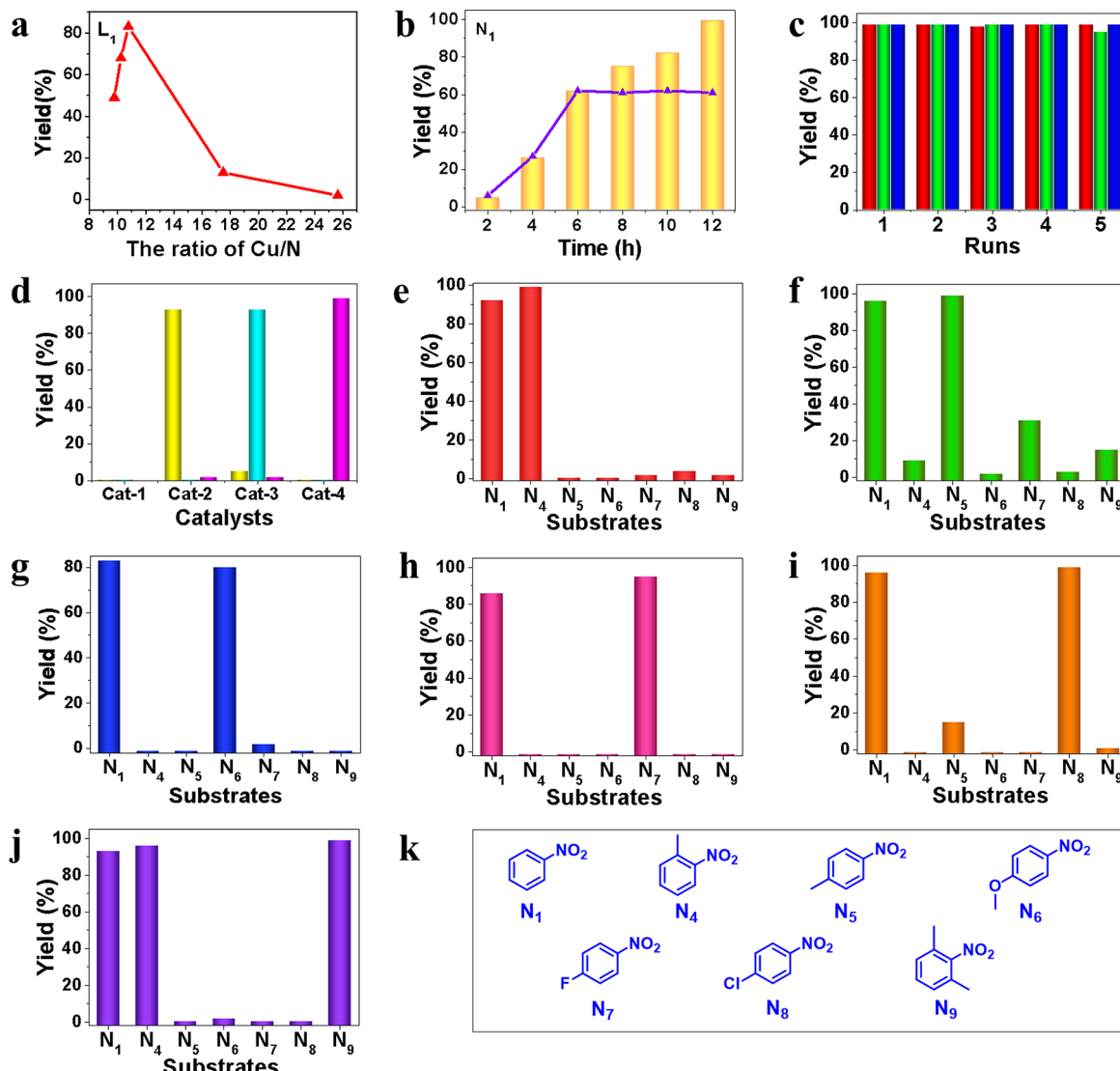


Figure 6. Catalytic performance of MICs. (a) Volcano-type relationship between the Cu/N ratio and yield (details see Tables S1 and S2), (b) thermal filtration experiment and hydrogenation of N₁ over Cu/Al₂O₃-N₁-L₁ (histogram for time-yield and curve for thermal filtration experiment). (c) Catalytic performance of MICs with five cycles (the red for Cu/Al₂O₃-N₁-L₁, the green for Cu/Al₂O₃-N₂-L₁ and the blue for Cu/Al₂O₃-N₃-L₁). (d) Catalytic performance of Cu/Al₂O₃ and MICs after 5 runs (catalysts: Cat-1 for Cu/Al₂O₃, Cat-2 for Cu/Al₂O₃-N₁-L₁-5 reused, Cat-3 for Cu/Al₂O₃-N₂-L₁-5 reused, and Cat-4 for Cu/Al₂O₃-N₃-L₁-5 reused. Substances: yellow for N₁, cyan for N₂, and pink for N₃). Catalytic performance of MICs for substances: (e) Cu/Al₂O₃-N₄-L₁, (f) Cu/Al₂O₃-N₅-L₁, (g) Cu/Al₂O₃-N₆-L₁, (h) Cu/Al₂O₃-N₇-L₁, (i) Cu/Al₂O₃-N₈-L₁, (j) Cu/Al₂O₃-N₉-L₁, and (k) structure for substrates of N₁ and N₄-N₉). All yields of nitro compounds to anilines were determined by calibrated GC-FID using diphenyl as standard. Reaction condition: nitro compound (1 mmol), catalyst (80 mg, 4.2 wt % Cu), toluene (4 mL), 1.5 MPa H₂, 120 °C, 12 h.

Cu-N bonding, compared with the Cu foil (Cu–Cu, 8.0 Å⁻¹), Cu₂O (Cu–O, 7.2 Å⁻¹), and CuO (Cu–O, 6.3 Å⁻¹).^{48,49} Importantly, the signal of Cu-N bonding also appeared in Cu/Al₂O₃-N₁-L₁-used, indicating the stability of Cu-N sites (Figure S8).

In order to investigate the difference in H₂ activation ability between Cu/Al₂O₃ and Cu/Al₂O₃-N₁-L₁, H₂-TPR and N₂O pulse adsorption tests were performed. H₂-TPR curves of Cu/Al₂O₃, Cu/Al₂O₃-N₁-L₁, and Cu/Al₂O₃-N₁-L₁ used catalysts all showed three peaks in the range 100–800 °C which suggested three different H₂ chemisorption on catalysts (Figure 4c). Interestingly, the first reduction temperature of Cu/Al₂O₃-N₁-L₁ and Cu/Al₂O₃-N₁-L₁-used at 220 °C was lower than that of Cu/Al₂O₃ at 400 °C, indicating the stronger reduction ability of Cu/Al₂O₃-N₁-L₁.

In addition, the larger peak value and peak area of Cu/Al₂O₃-N₁-L₁ and Cu/Al₂O₃-N₁-L₁-used indicated that the MICs had more active sites to activate H₂. N₂O pulse titration experiment for Cu/Al₂O₃ showed weak chemisorption of N₂O even at the initial plus. However, Cu/Al₂O₃-N₁-L₁ and Cu/Al₂O₃-N₁-L₁ used showed stronger N₂O uptake ability consuming all N₂O at first plus under the identical conditions (Figure 4d). These results indicated that new active Cu-N sites were generated after the MI strategy.

3.3. Mechanism Investigation. Characterizations and experimental results indicated that MICs could not only improve the catalytic activity of nitro compounds hydrogenation via the formation of new active Cu-N sites but also promote the selectivity by the fabrication of imprinting cavity via MI strategy. To investigate the origin of the molecular imprinting effect of the enhanced catalytic activity and

selectivity, DFT calculations were performed. Considering Cu/Al₂O₃-N₁-L₁ was synthesized by the sequential adsorption of N₁ and L₁ on reduced Cu/Al₂O₃, Cu(111) surface as the dominant crystal plane (Figure 3f) was adopted as model for further simulation. Notably, the size of Cu nanoparticles (>6 nm) was far larger than the (12 × 12) Cu(111) model on Cu/Al₂O₃-N₃-L₁ surface (30.27 Å × 30.27 Å), indicating the rational of the calculation configuration (Figure S10). Based on previous reports^{50,51} and our calculation results, both the imprinting molecule (N₁) and imprinting ligand (L₁) were preferred to adsorb on the metal surface in flat models, and the imprinting cavity was formed by the sequential adsorption of N₁ and L₁ on Cu/Al₂O₃, which was confirmed by the DFT calculations. Moreover, the formation of Cu-N sites by the coordination of surface Cu species with N species of L₁ was obtained after the adsorption of L₁ as shown in Figure 5a, which corresponded to our previous characterization results. Because the imprinting cavity on the catalyst surface had significant effects on the selective hydrogenation of nitro compounds, Cu/Al₂O₃-N₃-L₁ and Cu/Al₂O₃-N₂-L₁ rather than Cu/Al₂O₃-N₁-L₁ were chosen to investigate the adsorption energy (E_{ads}) of substances. In the presence of Cu/Al₂O₃-N₃-L₁, the E_{ads} values of N₁, N₂, and N₃ were presented in Figure 5b–d, where the adsorption energy was gradually reduced from -1.66 eV (N₁) to -2.18 eV (N₂) and then to -2.96 eV (N₃). Lower adsorption energy of N₃ led to its favorably adsorbed on the surface of Cu/Al₂O₃-N₃-L₁, although the imprinting cavity was enough for these three nitro compounds. Similarly, when using the Cu/Al₂O₃-N₂-L₁ catalyst (Figure 5e–g), N₂ was more preferred to adsorb in the formed imprinting cavity with an adsorption energy of -2.17 eV which was much higher than that for N₁ (-1.66 eV). Obviously, the size of the imprinting cavity on Cu/Al₂O₃-N₂-L₁ was smaller than that for N₃, and its adsorption was excluded (Figure 5h). These results clarified the reason why enhanced selectivity was obtained by these MICs.

To investigate the origin of the enhanced catalytic activity, H₂ activation was studied as shown in Figure 5i. In the presence of bare Cu (IS-A), the adsorption energy of H₂ was -0.08 eV and the dissociation barrier for H₂ activation was 0.52 eV (Figure S11a). Notably, no matter at the center site of the cavity (IS-B) or at the Cu/Al₂O₃-N₁-L₁ interface (IS-C), a much lower H₂ adsorption energy was obtained compared with bare Cu (IS-A). However, the dissociation barrier for H₂ activation at IS-C (0.26 eV) was significantly lower than that at IS-B (0.39 eV), indicating the H₂ activation was preferred to be occurred at the Cu/Al₂O₃-N₁-L₁ the interface (Figure S11b,c).

The lower dissociation barrier for H₂ activation at IS-C was probably ascribed to the formation of new active Cu-N sites. Considering the high yields of N₃, N₂, and N₁ hydrogenation on MICs, it was supposed that the interface between Cu and L₁ (Cu-N site) was the active site for the nitro compounds hydrogenation. Based on the DFT results, we were convinced that the formation of new active Cu-N sites and imprinting cavity by our MI strategy, leading to the promoted activity and selectivity on the hydrogenation of the nitro compounds.

The reaction order for H₂ activation with respect to H₂ pressure was ~0.53 (Figure S12c), indicating the H₂ was activated via homolytic pathway.⁵² This result was further confirmed by the DFT calculations where lower dissociation barrier for H₂ activation via homolytic pathway at the Cu/Al₂O₃-N₁-L₁ interface (IS-C).

The in situ FTIR/GC-MS was conducted to monitor the hydrogenation process. As shown in Figures S12 and S13, the intermediates of nitrosobenzene and phenylhydroxylamine were detected. The hydrogenation of N₁ was studied ex situ by ¹H NMR spectroscopy to monitor the reaction process (Figure S2S). The signals corresponding to H in N₁ (H_a) decreased gradually, while the peaks corresponding to the aniline (H_b and H_c) increased over time. Based on these results, a plausible reaction mechanism was proposed in Figure S12d.

3.4. Reactions over MICs. To investigate the influence of the content of L and active metals on the catalytic performance, the ratio of Cu to N for Cu/Al₂O₃-N₁-L₁ was tuned. As shown in Figure 6a, the Cu/N ratio and yield presented volcano-type relationship. 83% yield was obtained on the hydrogenation of N₁ when Cu/Al₂O₃-N₁-L₁ had a Cu/N ratio of 10.77. Subsequently, the relationship between reaction time and yield of N₁ hydrogenation reaction was measured with Cu/Al₂O₃-N₁-L₁, the yield-time histogram showed that the reaction speed was slow first and increasing gradually, and finally reached the complete transformation at 12 h (Figure 6b, yellow histogram). To test whether the active Cu species were leached from the bulk phase during the reaction, a leaching experiment was performed for three MICs samples. After hot filtration from the reaction mixture, the filtrate was analyzed by ICP-AES and only 0.12–0.29 ppm of Cu, close to the minimum detection limit of the instrument (0.1 ppm), was obtained (Table S8).

In addition, no further reaction was observed for 6 h in the filtrate after thermal filtration experiment, which confirmed the heterogeneous nature for MICs catalyst and the catalytically active species were not from the leaching metallic sites (Figure 6b, blue curve). The similar results were obtained on Cu/Al₂O₃-N₂-L₁ and Cu/Al₂O₃-N₃-L₁ (Figure S14). Besides, the copper loading in three MICs samples after five recycles showed no obvious change compared to fresh catalyst (Table S9).

To investigate the recyclability and stability of MICs, the catalyst was separated by centrifugation and washed 3 times by toluene. After being simply dried under vacuum at 80 °C, it was recovered and directly reused for the next run. As shown in Figure 6c, three typical MICs of Cu/Al₂O₃-N₁-L₁, Cu/Al₂O₃-N₂-L₁, and Cu/Al₂O₃-N₃-L₁ could be used for at least five catalytic cycles without significant decline in product yield, indicating the excellent stability of MICs and thus its potential for practical application. More importantly, these three MICs still exhibited outstanding molecule imprinting effects after five catalytic cycles with excellent catalytic activity and selectivity (Figure 6d), confirming the superior stability of the new active Cu-N sites and maintenance of the imprinting cavity formed by N and L₁. Notably, DFT calculation revealed that the adsorption energy of nitrobenzene ($E_{ads} = -1.74$ eV) was lower than that of aniline ($E_{ads} = -1.66$ eV), indicating the easy removal of aniline and beneficial recovery of active sites. Moreover, it could be found that various batches of MICs which were prepared at different times using the same method and procedure exhibited good molecular imprinting effects, implying the reproducibility of this catalytic system (Table S12).

In order to investigate the generality of this synthesis protocol for MICs, this strategy was extended to manufacture Cu/Al₂O₃ with L₁ of other imprinting molecule (N₄–N₉, shown in Figure 6e–j) under the similar conditions. Using 2-

methylnitrobenzene (N_4), 4-methylnitro-benzene (N_5), 4-methoxynitrobenzene (N_6) bearing electron-donating functional groups as imprinting molecular, the resulting MICs catalysts such as $Cu/Al_2O_3-N_4-L_1$, $Cu/Al_2O_3-N_5-L_1$, $Cu/Al_2O_3-N_6-L_1$, exhibited improved catalytic activity and selectivity toward the hydrogenation of imprinting nitro molecular (Figure 6e–g). Moreover, MICs of $Cu/Al_2O_3-N_7-L_1$ and $Cu/Al_2O_3-N_8-L_1$ derived from electron-withdrawing 4-fluoronitrobenzene (N_7) and 4-chloronitrobenzene (N_8) were also successfully constructed and catalyzed the hydrogenation of N_7 and N_8 with 96% and 99% yield, respectively (Figure 6h,i). As expected, all catalysts were active for nitrobenzene (N_1) hydrogenation with 81–96% yield because the sizes of each resulting imprinting cavity covered the sizes of the nitrobenzene. Importantly, all catalysts were almost not active for other substrates except N_1 even with subtle structure change, suggesting the formation of a precise imprinting cavity. Interestingly, it should be noted that $Cu/Al_2O_3-N_9-L_1$ catalyst from 2,6-dimethylnitrobenene (N_9) displayed 98% yield for the hydrogenation of N_9 (Figure 6j), while nitrobenzene (N_1) and 2-methylnitro-benzene (N_4) rather than other substances (N_5-N_8) were smoothly transformed to the desired amine with excellent yield at the same reaction condition. These results indicated that the molecular sizes of N_1 and N_4 could match the imprinting cavity of $Cu/Al_2O_3-N_9-L_1$ and then activated by the new formed Cu-N active sites, leading the excellent activity and selectivity toward the N_1 and N_4 hydrogenation. What's more, MICs derived from more steric imprinting molecules such as 2-methyl-1-nitrothalene (N_{10}) and 5-bromo-1-nitronaphthalene (N_{11}) were successfully prepared and the corresponding imprinting molecules were selectively hydrogenated to the amines with 98% and 81% yield only using the corresponding MICs, respectively (Figure S15). These results further validated the generality of this strategy to prepare versatile MICs.

4. CONCLUSIONS

In summary, we demonstrated a strategy to prepare MICs through a sequential adsorption of imprinting molecule (nitro compounds, N) and imprinting ligand (1,10-phenanthroline, L₁) on Cu/Al_2O_3 . The resulting MICs exhibited excellent molecule imprinting effects by the formation of new active Cu-N sites and precise imprinting cavities, endowing them promoted catalytic activity and selectivity on the hydrogenation of nitro compounds. Characterizations such as TGA, XRD, XPS, XAFS, H₂-TPR, and N₂O plus were conducted to clarify the formation of Cu-N sites, and experimental studies proved the formation of the imprinting cavities by the selective hydrogenation of the imprinting molecule. Furthermore, DFT calculations disclosed the origin of the enhanced activity and selectivity where the H₂ activation activity was beneficial by the new Cu-N sites, and the adsorption of imprinting molecules was preferred on the formed precise imprinting cavity. Finally, our strategy exhibited excellent generality to prepare versatile MICs by simply changing the imprinting molecules with outstanding catalytic activity and selectivity on hydrogenation. Our work provided a new strategy to synthesis MICs with not only imprinting cavities (reason for high selectivity) but also new active sites (origin for high activity).

■ ASSOCIATED CONTENT

SI Supporting Information

The Supporting Information is available free of charge at <https://pubs.acs.org/doi/10.1021/jacs.3c04576>.

Complete experimental procedures and characterization data for the prepared catalysts, including Figures of XPS spectra, TEM images, XRD patterns, UV-Raman spectrum, the data of ICP-AES, EA, and N₂ adsorption–desorption, DFT images, description of the XAS model tables with the obtained fitting parameters and detailed experimental section (PDF)

■ AUTHOR INFORMATION

Corresponding Authors

Feng Shi – State Key Laboratory for Oxo Synthesis and Selective Oxidation, Lanzhou Institute of Chemical Physics, Chinese Academy of Sciences, Lanzhou 730000, China;
ORCID: [0000-0001-5665-4933](https://orcid.org/0000-0001-5665-4933); Email: fshi@licp.ac.cn

Xinjiang Cui – State Key Laboratory for Oxo Synthesis and Selective Oxidation, Lanzhou Institute of Chemical Physics, Chinese Academy of Sciences, Lanzhou 730000, China;
ORCID: [0000-0002-3656-1139](https://orcid.org/0000-0002-3656-1139); Email: xinjiangcui@licp.ac.cn

Authors

Dongcheng He – State Key Laboratory for Oxo Synthesis and Selective Oxidation, Lanzhou Institute of Chemical Physics, Chinese Academy of Sciences, Lanzhou 730000, China;
University of Chinese Academy of Sciences, Beijing 100049, China

Teng Li – State Key Laboratory for Oxo Synthesis and Selective Oxidation, Lanzhou Institute of Chemical Physics, Chinese Academy of Sciences, Lanzhou 730000, China

Xingchao Dai – State Key Laboratory for Oxo Synthesis and Selective Oxidation, Lanzhou Institute of Chemical Physics, Chinese Academy of Sciences, Lanzhou 730000, China

Shujuan Liu – State Key Laboratory for Oxo Synthesis and Selective Oxidation, Lanzhou Institute of Chemical Physics, Chinese Academy of Sciences, Lanzhou 730000, China

Complete contact information is available at:
<https://pubs.acs.org/10.1021/jacs.3c04576>

Author Contributions

The manuscript was written through contributions of all authors. All authors have given approval to the final version of the manuscript.

Notes

The authors declare no competing financial interest.

■ ACKNOWLEDGMENTS

We thank the National Natural Science Foundation of China (Nos. 21925207 and 22102195), the Natural Science Foundation of Gansu Province, China and the Major Project of Gansu Province, China (Nos. 21JR7RA096 and 21ZD4WA021) for the financial supports. The XAFS beam time was granted by 1W1B end station of Beijing Synchrotron Radiation Facility (1W1B, BSRF), Institute of High Energy Physics, Chinese Academy of Sciences. We thank Prof. Dr. Lirong Zheng (Institute of High Energy Physics, CAS) and other staff members of 1W1B for their support in measurements and data reduction.

■ REFERENCES

- (1) Zaera, F. Designing Sites in Heterogeneous Catalysis: Are We Reaching Selectivities Competitive With Those of Homogeneous Catalysts? *Chem. Rev.* **2022**, *122* (9), 8594–8757.
- (2) Wang, C. F.; Zhang, L.; Huang, X.; Zhu, Y. F.; Li, G.; Gu, Q. F.; Chen, J. Y.; Ma, L. G.; Li, X. J.; He, Q. H.; et al. Maximizing Sinusoidal Channels of HZSM-5 for High Shape-Selectivity to p-Xylene. *Nat. Commun.* **2019**, *10*, 4348–4355.
- (3) Lee, W. T.; van Muyden, A. P.; Bobbink, F. D.; Huang, Z.; Dyson, P. J. Indirect CO₂Methanation: Hydrogenolysis of Cyclic Carbonates Catalyzed by Ru-Modified Zeolite Produces Methane and Diols. *Angew. Chem., Int. Ed.* **2019**, *58* (2), 557–560.
- (4) Lee, W. T.; van Muyden, A.; Bobbink, F. D.; Mensi, M. D.; Carullo, J. R.; Dyson, P. J. Mechanistic Classification and Benchmarking of Polyolefin Depolymerization over Silica-Alumina-Based Catalysts. *Nat. Commun.* **2022**, *13* (1), 4850–4862.
- (5) Wang, C. T.; Fang, W.; Liu, Z. Q.; Wang, L.; Liao, Z. W.; Yang, Y. R.; Li, H. J.; Liu, L.; Zhou, H.; Qin, X. D.; Xu, S. D.; Chu, X. F.; Wang, Y. Q.; Zheng, A. M.; Xiao, F. S. Fischer–Tropsch Synthesis to Olefins Boosted by MFI Zeolite Nanosheets. *Nat. Nanotechnol.* **2022**, *17* (7), 714–720.
- (6) Howarth, A. J.; Liu, Y. Y.; Li, P.; Li, Z. Y.; Wang, T. C.; Hupp, J.; Farha, O. K. Chemical, Thermal and Mechanical Stabilities of Metal-Organic Frameworks. *Nat. Rev. Mater.* **2016**, *1* (3), 15018–15032.
- (7) Marshall, S. T.; O'Brien, M.; Oetter, B.; Corpuz, A.; Richards, R. M.; Schwartz, D. K.; Medlin, J. W. Controlled Selectivity for Palladium Catalysts Using Self-Assembled Monolayers. *Nat. Mater.* **2010**, *9* (10), 853–858.
- (8) Xu, H. S.; Ding, S. Y.; An, W.-K.; Wu, H.; Wang, W. Constructing Crystalline Covalent Organic Frameworks from Chiral Building Blocks. *J. Am. Chem. Soc.* **2016**, *138* (36), 11489–11492.
- (9) Willis, J. J.; Goodman, E. D.; Wu, L.; Riscoe, A. R.; Martins, P.; Tassone, C. J.; Cargnello, M. Systematic Identification of Promoters for Methane Oxidation Catalysts Using Size- and Composition-Controlled Pd-Based Bimetallic Nanocrystals. *J. Am. Chem. Soc.* **2017**, *139* (34), 11989–11997.
- (10) Gao, Z.; Wang, G.; Lei, T.; Lv, Z.; Xiong, M.; Wang, L.; Xing, S.; Ma, J.; Jiang, Z.; Qin, Y. Enhanced Hydrogen Generation by Reverse Spillover Effects over Bicomponent Catalysts. *Nat. Commun.* **2022**, *13* (1), 118–126.
- (11) Yuan, Y.; Yan, N.; Dyson, P. J. Advances in the Rational Design of Rhodium Nanoparticle Catalysts: Control via Manipulation of the Nanoparticle Core and Stabilizer. *ACS Catal.* **2012**, *2* (6), 1057–1069.
- (12) Lang, R.; Du, X. R.; Huang, Y. K.; Jiang, X. Z.; Zhang, Q.; Guo, Y. L.; Liu, K. P.; Qiao, B. T.; Wang, A. Q.; Zhang, T. Single-Atom Catalysts Based on the Metal-Oxide Interaction. *Chem. Rev.* **2020**, *120* (21), 11986–12043.
- (13) Song, S.; Qu, J. F.; Han, P. J.; Hulsey, M. J.; Zhang, G. P.; Wang, Y. Z.; Wang, S.; Chen, D. Y.; Lu, J. M.; Yan, N. Visible-Light-Driven Amino Acids Production from Biomass-Based Feedstocks over Ultrathin CdS Nanosheets. *Nat. Commun.* **2020**, *11* (1), 4899–4908.
- (14) Chen, F.; Surkus, A. E.; He, L.; Pohl, M. M.; Radnik, J.; Topf, C.; Junge, K.; Beller, M. Selective Catalytic Hydrogenation of Heteroarenes with N-Graphene-Modified Cobalt Nanoparticles (Co₃O₄ Co/NGr@alpha-Al₂O₃). *J. Am. Chem. Soc.* **2015**, *137* (36), 11718–11724.
- (15) Jagadeesh, R. V.; Surkus, A. E.; Junge, H.; Pohl, M. M.; Radnik, J.; Rabeah, J.; Huan, H. M.; Schunemann, V.; Bruckner, A.; Beller, M. Nanoscale Fe₂O₃-Based Catalysts for Selective Hydrogenation of Nitroarenes to Anilines. *Science* **2013**, *342* (6162), 1073–1076.
- (16) Li, Z.; Ji, S. F.; Liu, Y. W.; Cao, X.; Tian, S. B.; Chen, Y. J.; Niu, Z. G.; Li, Y. D. Well-Defined Materials for Heterogeneous Catalysis: From Nanoparticles to Isolated Single-Atom Sites. *Chem. Rev.* **2020**, *120* (2), 623–682.
- (17) van Deelen, T. W.; Hernández Mejía, C. H.; de Jong, K. P. Control of Metal-Support Interactions in Heterogeneous Catalysts to Enhance Activity and Selectivity. *Nat. Catal.* **2019**, *2* (11), 955–970.
- (18) Xiong, M.; Gao, Z.; Zhao, P.; Wang, G. F.; Yan, W. J.; Xing, S. F.; Wang, P. F.; Ma, J. Y.; Jiang, Z.; Liu, X. C.; et al. In Situ Tuning of Electronic Structure of Catalysts Using Controllable Hydrogen Spillover for Enhanced Selectivity. *Nat. Commun.* **2020**, *11* (1), 4773–4782.
- (19) Zhang, B.; Sun, G.; Ding, S. P.; Asakura, H.; Zhang, J.; Sautet, P.; Yan, N. Atomically Dispersed Pt-1-Polyoxometalate Catalysts: How Does Metal-Support Interaction Affect Stability and Hydrogenation Activity? *J. Am. Chem. Soc.* **2019**, *141* (20), 8185–8197.
- (20) Han, B.; Guo, Y.; Huang, Y.; Xi, W.; Xu, J.; Luo, J.; Qi, H.; Ren, Y.; Liu, X.; Qiao, B.; Zhang, T. Strong Metal-Support Interactions between Pt Single Atoms and TiO₂. *Angew. Chem., Int. Ed.* **2020**, *59* (29), 11824–11829.
- (21) Coperet, C.; Chabanas, M.; Petroff Saint-Arroman, R.; Basset, J. M. Homogeneous and Heterogeneous Catalysis: Bridging the Gap Through Surface Organometallic Chemistry. *Angew. Chem., Int. Ed.* **2003**, *42* (2), 156–181.
- (22) Ortega Lorenzo, M.; Baddeley, C. J.; Muryn, C.; Raval, R. Extended Surface Chirality from Supramolecular Assemblies of Adsorbed Chiral Molecules. *Nature* **2000**, *404* (6776), 376–379.
- (23) Zhang, S. F.; Zhang, B.; Liang, H. J.; Liu, Y. Q.; Qiao, Y.; Qin, Y. Encapsulation of Homogeneous Catalysts in Mesoporous Materials Using Diffusion-Limited Atomic Layer Deposition. *Angew. Chem., Int. Ed.* **2018**, *57* (4), 1091–1095.
- (24) Westerhaus, F. A.; Jagadeesh, R. V.; Wienhofer, G.; Pohl, M. M.; Radnik, J.; Surkus, A. E.; Rabeah, J.; Junge, K.; Junge, H.; Nielsen, M.; Bruckner, A.; Beller, M. Heterogenized Cobalt Oxide Catalysts for Nitroarene Reduction by Pyrolysis of Molecularly Defined Complexes. *Nat. Chem.* **2013**, *5* (6), 537–543.
- (25) Luo, M.; Yang, J. T.; Li, X. G.; Eguchi, M.; Yamauchi, Y.; Wang, Z. L. Insights into alloy/oxide or hydroxide interfaces in Ni-Mo-based electrocatalysts for hydrogen evolution under alkaline conditions. *Chem. Sci.* **2023**, *14* (13), 3400–3414.
- (26) Zhang, Z. Y.; Bian, L.; Tian, H.; Liu, Y.; Bando, Y.; Yamauchi, Y.; Wang, Z. L. Tailoring the Surface and Interface Structures of Copper-Based Catalysts for Electrochemical Reduction of CO₂ to Ethylene and Ethanol. *Small* **2022**, *18* (18), 2107450–21074473.
- (27) Zhang, L.; Zhou, M.; Wang, A.; Zhang, T. Selective Hydrogenation over Supported Metal Catalysts: From Nanoparticles to Single Atoms. *Chem. Rev.* **2020**, *120* (2), 683–733.
- (28) Singh, B.; Gawande, M. B.; Kute, A. D.; Varma, R. S.; Fornasiero, P.; McNeice, P.; Jagadeesh, R. V.; Beller, M.; Zboril, R. Single-Atom (Iron-Based) Catalysts: Synthesis and Applications. *Chem. Rev.* **2021**, *121* (21), 13620–13697.
- (29) Hulsey, M. J.; Zhang, B.; Ma, Z. R.; Asakura, H.; Do, D. A.; Chen, W.; Tanaka, T.; Zhang, P.; Wu, Z. L.; Yan, N. In Situ Spectroscopy-Guided Engineering of Rhodium Single-Atom Catalysts for CO Oxidation. *Nat. Commun.* **2019**, *10*, 1330–1339.
- (30) Guo, Y. L.; Li, Y. Y.; Du, X. R.; Li, L.; Jiang, Q. K.; Qiao, B. T. Pd Single-Atom Catalysts Derived from Strong Metal-Support Interaction for Selective Hydrogenation of Acetylene. *Nano Res.* **2022**, *15* (12), 10037–10043.
- (31) Wang, X.; Li, J.; Chen, L. Advanced Preparation Technologies and Strategies for Molecularly Imprinted Materials. *Chin. Sci. Bull.* **2019**, *64* (13), 1352–1367.
- (32) Chen, L. X.; Wang, X. Y.; Lu, W. H.; Wu, X. Q.; Li, J. H. Molecular Imprinting: Perspectives and Applications. *Chem. Soc. Rev.* **2016**, *45* (8), 2137–2211.
- (33) Cutivet, A.; Schembri, C.; Kovensky, J.; Haupt, K. Molecularly Imprinted Microgels as Enzyme Inhibitors. *J. Am. Chem. Soc.* **2009**, *131* (41), 14699–14702.
- (34) Hoshino, Y.; Koide, H.; Urakami, T.; Kanazawa, H.; Kodama, T.; Oku, N.; Shea, K. J. Recognition, Neutralization, and Clearance of Target Peptides in the Bloodstream of Living Mice by Molecularly Imprinted Polymer Nanoparticles: A Plastic Antibody. *J. Am. Chem. Soc.* **2010**, *132* (19), 6644–6645.
- (35) Brunkan, N. M.; Gagne, M. R. Effect of Chiral Cavities Associated with Molecularly Imprinted Platinum Centers on the

Selectivity of Ligand-Exchange Reactions at Platinum. *J. Am. Chem. Soc.* **2000**, *122* (26), 6217–6225.

(36) Katz, A.; Davis, M. E. Molecular Imprinting of Bulk, Microporous Silica. *Nature* **2000**, *403* (6767), 286–289.

(37) Canlas, C. P.; Lu, J. L.; Ray, N. A.; Grosso-Giordano, N. A.; Lee, S.; Elam, J. W.; Winans, R. E.; Van Duyne, R. P.; Stair, P. C.; Notestein, J. M. Shape-Selective Sieving Layers on an Oxide Catalyst Surface. *Nat. Chem.* **2012**, *4* (12), 1030–1036.

(38) Wu, D.; Baaziz, W.; Gu, B.; Marinova, M.; Hernandez, W. Y.; Zhou, W.; Vovk, E. I.; Ersen, O.; Safonova, O. V.; Addad, A.; Nuns, N.; Khodakov, A. Y.; Ordomsky, V. V. Surface Molecular Imprinting over Supported Metal Catalysts for Size-Dependent Selective Hydrogenation Reactions. *Nat. Catal.* **2021**, *4* (7), 595–606.

(39) Liu, X.; Zhu, Q.; Lang, Y.; Cao, K.; Chu, S.; Shan, B.; Chen, R. Oxide-Nanotrap-Anchored Platinum Nanoparticles with High Activity and Sintering Resistance by Area-Selective Atomic Layer Deposition. *Angew. Chem., Int. Ed.* **2017**, *56* (6), 1648–1652.

(40) Koy, M.; Bellotti, P.; Das, M.; Glorius, F. N-Heterocyclic Carbenes as Tunable Ligands for Catalytic Metal Surfaces. *Nat. Catal.* **2021**, *4* (5), 352–363.

(41) Bellotti, P.; Koy, M.; Hopkinson, M. N.; Glorius, F. Recent advances in the chemistry and applications of N-heterocyclic carbenes. *Nat. Rev. Chem.* **2021**, *5* (10), 711–725.

(42) Ernst, J. B.; Schwermann, C.; Yokota, G.-I.; Tada, M.; Muratsugu, S.; Doltsinis, N. L.; Glorius, F. Molecular Adsorbates Switch on Heterogeneous Catalysis: Induction of Reactivity by N-Heterocyclic Carbenes. *J. Am. Chem. Soc.* **2017**, *139* (27), 9144–9147.

(43) Wang, B. Q.; Cheng, C.; Jin, M. M.; He, J.; Zhang, H.; Ren, W.; Li, J.; Wang, D. S.; Li, Y. D. A Site Distance Effect Induced by Reactant Molecule Matchup in Single-Atom Catalysts for Fenton-Like Reactions. *Angew. Chem., Int. Ed.* **2022**, *61* (33), e202207268.

(44) Choy, J.-H.; Yoon, J.-B.; Jung, H. Polarization-Dependent X-ray Absorption Spectroscopic Study of [Cu(cyclam)]²⁺-Intercalated Saponite. *J. Phys. Chem. B* **2002**, *106* (43), 11120–11126.

(45) Cui, G.; Zhang, X.; Wang, H.; Li, Z.; Wang, W.; Yu, Q.; Zheng, L.; Wang, Y.; Zhu, J.; Wei, M. ZrO₂-Modified Cu Nanocatalysts with Synergistic Catalysis Towards Carbon-Oxygen Bond Hydrogenation. *Appl. Catal. B: Environ.* **2021**, *280*, 119406–119416.

(46) Wu, Y. J.; Huang, Y. J.; Dai, X. C.; Shi, F. Alcohol Amination Catalyzed by Copper Powder as a Self-Supported Catalyst. *ChemSusChem* **2019**, *12* (13), 3185–3191.

(47) Niu, W.; Li, L.; Liu, X.; Wang, N.; Liu, J.; Zhou, W.; Tang, Z.; Chen, S. Mesoporous N-doped Carbons Prepared with Thermally Removable Nanoparticle Templates: an Efficient Electrocatalyst for Oxygen Reduction Reaction. *J. Am. Chem. Soc.* **2015**, *137* (16), 5555–5562.

(48) Wang, T.; Yang, R.; Shi, N.; Yang, J.; Yan, H.; Wang, J.; Ding, Z.; Huang, W.; Luo, Q.; Lin, Y.; Gao, J.; Han, M. Cu,N-Codoped Carbon Nanodisks With Biomimic Stomata-Like Interconnected Hierarchical Porous Topology as Efficient Electrocatalyst for Oxygen Reduction Reaction. *Small* **2019**, *15* (43), 1902410–1902420.

(49) Han, X.; Zhang, T. Y.; Wang, X. H.; Zhang, Z. D.; Li, Y. P.; Qin, Y. J.; Wang, B. Q.; Han, A. J.; Liu, J. F. Hollow Mesoporous Atomically Dispersed Metal-Nitrogen-Carbon Catalysts with Enhanced Diffusion for Catalysis Involving Larger Molecules. *Nat. Commun.* **2022**, *13* (1), 2900–2908.

(50) He, D.; Wang, T.; Li, T.; Wang, X.; Wang, H.; Dai, X.; Shi, F. Efficient Hydrogenation Catalyst Designing via Preferential Adsorption Sites Construction Towards Active Copper. *J. Catal.* **2021**, *400*, 397–406.

(51) Chen, G. X.; Xu, C. F.; Huang, X. Q.; Ye, J. Y.; Gu, L.; Li, G.; Tang, Z. C.; Wu, B. H.; Yang, H. Y.; Zhao, Z. P.; Zhou, Z. Y.; Fu, G.; Zheng, N. F. Interfacial Electronic Effects Control the Reaction Selectivity of Platinum Catalysts. *Nat. Mater.* **2016**, *15* (5), 564–569.

(52) Kubas, G. J. Fundamentals of H-2 binding and reactivity on transition metals underlying hydrogenase function and H-2 production and storage. *Chem. Rev.* **2007**, *107* (10), 4152–4205.